**Pushing the boundaries of chemistry?
It takes
#HumanChemistry**

Make your curiosity and talent as a chemist matter to the world with a specialty chemicals leader. Together, we combine cutting-edge science with engineering expertise to create solutions that answer real-world problems. Find out how our approach to technology creates more opportunities for growth, and see what chemistry can do for you at:

evonik.com/career

EVONIK
Leading Beyond Chemistry

Active and passive tuning of ultra-narrow resonances in polaritonic nanoantennas

J. Duan*, F.J. Alfaro-Mozaz , J. Taboada-Gutiérrez, I. Dolado, G. Álvarez-Pérez, Elena Titova, A. Bylinkin, A. I. F. Tresguerres-Mata, J. Martín-Sánchez, S. Liu, J.H. Edgar, D.A. Bandurin, P. Jarillo-Herrero, R. Hillenbrand, A.Y. Nikitin*, and P. Alonso-González*

Dr. J. Duan, J. Taboada-Gutiérrez, G. Álvarez-Pérez, A. I. F. Tresguerres-Mata, Dr. J. Martín-Sánchez, Dr. P. Alonso-González

Department of Physics

University of Oviedo

Oviedo 33006, Spain

Email: duanjiahua@uniovi.es, pabloalonso@uniovi.es

Dr. J. Duan, J. Taboada-Gutiérrez, G. Álvarez-Pérez, A. I. F. Tresguerres-Mata, Dr. J. Martín-Sánchez, Dr. P. Alonso-González

Center of Research on Nanomaterials and Nanotechnology

CINN (CSIC-Universidad de Oviedo)

El Entrego 33940, Spain

Dr. F.J. Alfaro-Mozaz, I. Dolado, A. Bylinkin

CIC nanoGUNE BRTA

Donostia-San Sebastian 20018, Spain

Elena Titova

Programmable functional materials lab, Brain and Consciousness research center, Moscow, Russia

Elena Titova

Center for Photonics and 2D materials, Moscow Institute of Physics and Technology, Dolgoprudny, Russia

A. Bylinkin, Dr. A.Y. Nikitin

Donostia International Physics Center (DIPC)

Donostia-San Sebastian 20018, Spain

Email: alexey@dipc.org

Dr. S. Liu, Dr. J.G. Edgar

Tim Taylor Department of Chemical Engineering

Kansas State University

Manhattan, KS 66506 USA

Dr. D.A. Bandurin, Dr. P. Jarillo-Herrero

Department of Physics

Massachusetts Institute of Technology

Boston, MA, 02139, USA

Dr. R. Hillenbrand, Dr. A.Y. Nikitin

IKERBASQUE

Basque Foundation for Science

Bilbao 48013, Spain

Dr. R. Hillenbrand

CIC nanoGUNE BRTA and Department of Electricity and electronics, EHU/UPV

Donostia-San Sebastián, 20018, Spain

Abstract

Optical nanoantennas are of great importance for photonic devices and spectroscopy due to their capability to squeeze light at the nanoscale and enhance light-matter interactions. Among them, nanoantennas made of polar crystals supporting phonon polaritons (phononic nanoantennas) exhibit the highest quality factors. This is due to the low optical losses inherent in these materials, which, however, hinder the spectral tuning of the nanoantennas due to their dielectric nature. Here we realize active and passive tuning of ultra-narrow resonances in phononic nanoantennas over a wide spectral range (~35 cm^{-1}, being the resonance linewidth ~9 cm^{-1}), monitored by near-field nanoscopy. To do that, we modify the local environment of a single nanoantenna made of hexagonal boron nitride (h-BN) by placing it on different polar substrates, such as quartz (SiO$_2$) and silicon carbide (4H-SiC), or covering it with layers of a high refractive-index van der Waals crystal (WSe$_2$). Importantly, we demonstrate active tuning of the nanoantenna polaritonic resonances by placing it

3

on top of a gated graphene monolayer in which we vary the Fermi energy. Our work presents the realization of tunable polaritonic nanoantennas with ultra-narrow resonances, which could find applications in active nanooptics and (bio)-sensing.

1. Introduction

Polaritons[1, 2, 3], light coupled to coherently oscillating charges, enable strong enhancement and confinement of electromagnetic fields at dimensions deep below the incident wavelength. They are thus attractive for numerous applications, such as nanoscale light-trapping[4], single molecule sensing[5, 6, 7] or photo-detection[8]. Typically, plasmon polaritons—collective oscillations of free electrons coupled to photons—at metal or semiconductor surfaces have been employed to design plasmonic antennas for light manipulation[9, 10] and enhanced spectroscopy[11-13]. However, the problems of large absorption losses[14, 15] and lack of active tunability impose severe limitations to manipulate plasmon polaritons in metals. As a promising alternative, the semimetal graphene has recently opened new opportunities for the development of active subwavelength-scale optics[16, 17] and robust plasmonic biosensors[18] due to its tunable plasmonic response[19, 20] and high degree of light confinement[21-23]. On the other hand, phonon polaritons (PhPs) [24] – hybrid waves resulting from the coupling of crystal lattice vibrations and photons - have been far less studied compared to their plasmonic counterparts. However, PhPs-based phononic nanoantennas provide significantly improved field enhancements and quality factors[25-28] compared to plasmonic nanoantennas due to the suppression of ohmic losses. Some van der Waals (vdW) materials[29-31] exhibit mid-infrared PhPs with a record-high lifetime (up to 20 picoseconds) in the so-called reststrahlen bands, defined as the

frequency region between the transverse optical (TO) and longitudinal optical (LO) phonons and in which the dielectric permittivity is negative, hence enabling the existence of polaritonic modes. For instance, hexagonal boron nitride (h-BN) is a uniaxial hyperbolic vdW material[32], whose real-part of the parallel ($\varepsilon_\parallel$) and perpendicular ($\varepsilon_\perp$) dielectric permittivities have opposite signs. This optical property of h-BN enables the propagation of low-loss PhPs featuring hyperbolic dispersion and large density of optical states, which is important for strong field confinement[33, 34] and enhancement of light-matter interactions[25]. Large quality factor (*Q*) PhP resonances in h-BN cone-shaped and linear (dipolar) nanoantennas have been demonstrated by recent nano-spectroscopy experiments[25, 28, 35], revealing the broad application prospects of phononic nanoantennas made of hyperbolic materials in infrared (IR) nanophotonics (*e.g.* for refractive index sensing[28] or surface-enhanced infrared absorption spectroscopy[36, 37]). However, since the properties of PhPs are dictated by the crystal lattice dynamics, spectral tuning of PhPs is challenging. Although control of the dispersion of propagating PhPs was achieved by combining h-BN slabs with gated graphene[38, 39], spectral tuning of the resonances in phononic nanoantennas remains elusive, yet it is very appealing due to their large *Q*.

Here we demonstrate active and passive tuning of ultra-narrow resonances in phononic nanoantennas, namely h-BN squares with a nanoscale cross-section. Our nanoimaging experiments and numerical simulations reveal sharp resonances with linewidths of around 9 cm^{-1} (*Q* ~ 165), which generate puzzling near-field patterns that allow shrinking mid-infrared light (of incident wavelength λ_0) to subwavelength dimensions (~λ_0/42). Passive tuning of these ultra-narrow resonances is demonstrated over several resonance linewidths by modifying the dielectric environment of the

phononic nanoantenna. This modification is realized by placing the nanoantenna on different substrates as well as covering it with different superstrates (without moving the nanoantenna). Importantly, we also demonstrate the realization of actively tunable nanoantennas with ultra-narrow resonances (linewidths of ~20 cm^{-1}, *i.e.* one order of magnitude smaller than the typical linewidths in active graphene nanoantennas) by placing them on top of gated graphene in which we vary the Fermi energy. Our results establish the basis for the control of polaritonic resonances in nanoantennas made of hyperbolic materials, while the combination of refractive-index sensitivity and active tunability of ultra-narrow resonances open exciting prospects for biosensing and the realization of tunable strong coupling phenomena at the nanoscale.

2. Infrared nanoimaging of square h-BN nanoantennas.

To study the polaritonic resonances in phononic nanoantennas made of vdW hyperbolic materials, we fabricate h-BN squares with a nanoscale cross-section and carry out near-field measurements by employing scattering-type scanning near-field optical microscopy (s-SNOM). To nanoimage the square h-BN nanoantennas, we illuminate the s-SNOM tip with p-polarized monochromatic mid-IR light and record the amplitude of the tip-scattered field as a function of the tip position (see schematics in **Figure 1a**). PhPs propagate radially outwards from the tip, reflect upon reaching the corners and edges of the nanoantennas, and modify the tip-scattered light when they return to the tip. By raster scanning the nanoantenna surface at different incident frequencies (ω_0), we observe complex near-field modal patterns with bright dots at the edges and a variety of features inside the nanoantenna (Figure 1b-1i). Interestingly, the near-field patterns change dramatically even with a

slight variation of ω_0. For instance, one single bright spot appearing in the center of the nanoantenna at ω_0=1490 cm^{-1} (Figure 1e), changes to a dark spot surrounded by a bright ring for a frequency shift of only 10 cm^{-1}, at ω_0=1500 cm^{-1} (Figure 1f). To study the origin of these near-field patterns, we extract the PhPs wavevector q by taking a line-profile in the experimental near-field amplitude images, both inside the nanoantennas (lower panels in Figure 1b-1i) and at their periphery (see Supplementary Information). We determine q by using the relation $q = \pi/L$, where L is the distance between the adjacent maxima in the amplitude line-profile[26]. When ω_0 increases from ω_0=1450 cm^{-1} (Figure 1b) to ω_0=1540 cm^{-1} (Figure 1i), the number of peaks (lower panels in Figure 1b-1i) gradually increases from one (Figure 1b) to seven (Figure 1i). Such a dramatic increase of the number of peaks is an important implication of a spectrally evolving standing wave pattern, clearly indicating a set of Fabry-Perot resonances, analogous to those emerging in h-BN linear antennas[26]. In Figure1j, we show the dispersion ω_0 (q) obtained from experiments (filled symbols) and electromagnetic simulations (solid lines) of the PhP modes in an infinite h-BN slab. Here, M0 (black solid line) and SM0 (red solid line) represent the fundamental volume PhP mode in semi-infinite h-BN slabs [40, 41] and fundamental surface-confined PhP mode at the edges of h-BN slabs[42], respectively. We find a very good agreement between the dispersion curve of the M0 and SM0 modes and the measured data points inside and at the periphery of the nanoantennas, respectively. Thus, we conclude that the combination of fundamental volume and surface-confined PhP modes are the cause of the Fabry-Perot resonances in the square h-BN nanoantennas.
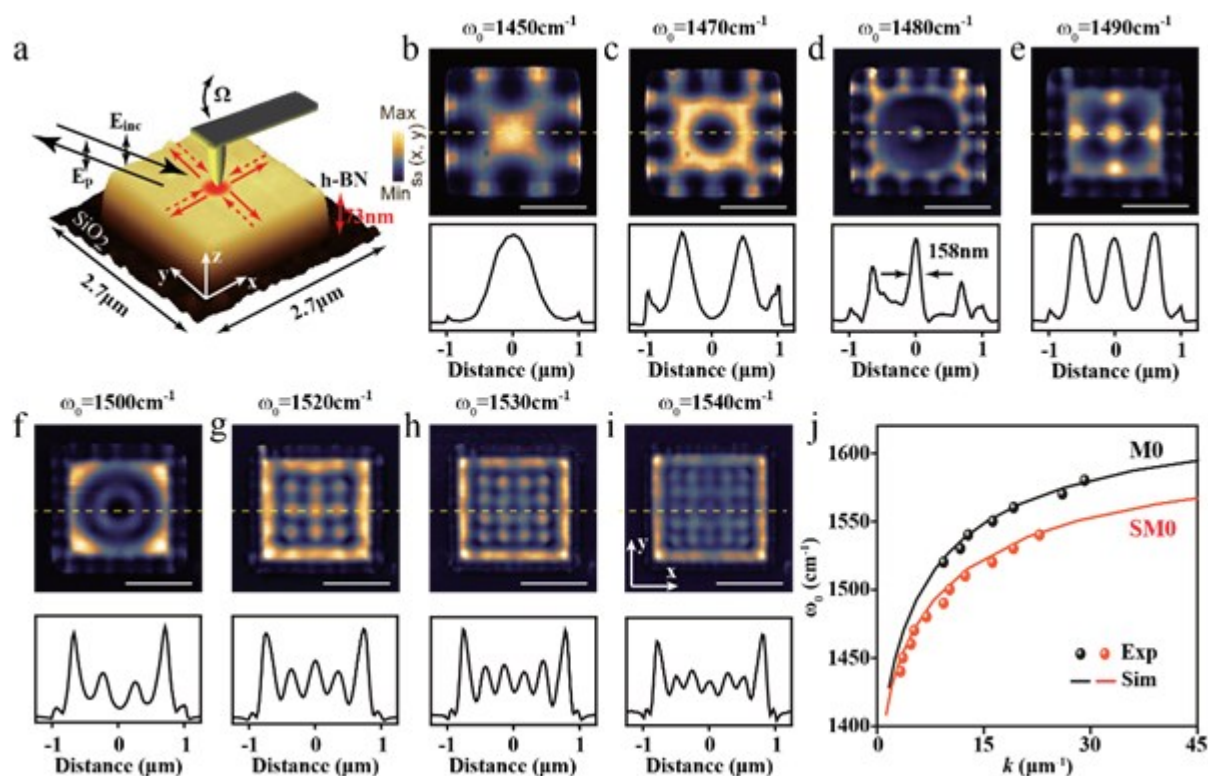
Figure 1. Real-space imaging of polaritonic modes in a square h-BN nanoantenna. (a) Schematics of the s-SNOM measurements of a square h-BN nanoantenna. (b-i) Upper panels: near-field images of the nanoantenna for incident frequencies (ω_0) of 1450cm⁻¹, 1470cm⁻¹, 1480cm⁻¹, 1490cm⁻¹, 1500cm⁻¹, 1520cm⁻¹, 1530cm⁻¹ and 1540cm⁻¹, respectively. Bottom panels: amplitude line-profiles extracted along the dashed lines in the near-field images. Scale bar: 1μm. (j) Simulated (solid lines) dispersions of the fundamental volume-confined (M0) and surface-confined (SM0) hyperbolic modes in a slab of h-BN. The solid symbols represent the experimental results extracted from line-profiles inside the nanoantenna (dashed line in b-i) and its periphery (Figure S3), respectively.

As expected for PhPs in h-BN in the reststrahlen band ($1395\,\mathrm{cm}^{-1} \leq \omega_0 \leq 1630\,\mathrm{cm}^{-1}$) [43], the wavevector q increases with ω_0 for both the M0 and SM0 modes, the latter showing a larger q (*i.e.* smaller wavelength). When ω_0 is larger than 1500 cm⁻¹ (Figure 1g-1i), the M0-PhPs wavelength is

much smaller than the side length (2 µm in this work) of the square h-BN nanoantenna and thus the latter exhibits a typical near-field pattern with periodic bright spots analogous to the case of large ("semi-infinite") h-BN slabs[40] and h-BN linear antennas[26]. However, for smaller ω_0, ranging from 1450 cm^{-1} (Figure 1b) to 1500 cm^{-1} (Figure 1f), the M0-PhPs wavelength becomes comparable with the side length of the square nanoantenna, introducing convoluted Fabry-Perot interferences featuring atypical near-field patterns. Therefore, the near-field patterns inside the square h-BN nanoantennas can be classified into two categories: atypical modal patterns (Figure 1b-1f) at relatively small ω_0, and typical periodic patterns (Figure 1g-1i) at large ω_0. On the other hand, the much smaller wavelength of the SM0 mode (always smaller than the side length) gives rise to periodic bright spots along the edges of the nanoantennas over the entire frequency range (Figure 1b-1i). Note that those atypical modal patterns (Figures 1b-1f) originating from Fabry-Perot resonances has remained elusive until now, since all previous works focused on the periodic patterns (e.g. fringes or periodic dots)[40,43-45] in the condition that the polariton wavelength is much smaller than the size of h-BN structures. However, some of those atypical patterns provides a nanoscale 'hot-spot' of deeply subwavelength dimensions ($\sim\lambda_0/42$) with respect to the incident mid-IR light (λ_0=6.76 µm). Such 'hot-spot' largely shrinks the huge gap between the IR light wavelength (of micrometer size) and the size of molecules (sub-nanometer size), and thus could enhance light-molecule interactions and find applications in molecular spectroscopy.

3. Modal analysis of Fabry-Perot resonances in square h-BN nanoantennas.

We further elaborate on the formation of near-field patterns in our square h-BN nanoantennas (Figure 1) by performing full-wave numerical simulations (see details in Methods). To do that, we approximate the s-SNOM tip by a vertical electric dipole source[46] which launches PhPs in the nanoantennas. For each in-plane location of the dipole, we plot the amplitude of the simulated out-of-plane component of the electric near-field ($|E_z|$) below the dipole as a function of frequency, as shown in **Figure 2a**. Such near-field spectra show a set of closely spaced peaks in a narrow spectral range, associated with the excitation of resonant Fabry-Perot modes. Different spectral positions of the peaks on different curves indicates that the excitation of PhP modes in the nanoantennas is strongly dependent on the dipole position. For instance, when the dipole is located at the center of the nanoantenna, the spectrum (black solid line in Figure 2a) shows five strong peaks (labelled as c1-c5), which correspond to five individual PhP modes. In contrast, when we locate the dipole at the corner of the nanoantenna, the spectrum (red solid line in Figure 2a) shows four discernable peaks (labelled as e1-e4). On the other hand, when the dipole is located at the flank of the nanoantenna (green solid line in Figure 2a) or its diagonal (purple solid line in Figure 2a), more peaks (labelled as s1-s6 or d1-d6) appear in the spectrum. To connect these near-field spectra with the experimental near-field images, we further simulate the $|E_z|$ as a function of the dipole position by raster scanning the dipole above a square h-BN nanoantenna for two different frequencies. At ω_0=1480 cm^{-1}, the experimental near-field image (Figure 2b, left panel) of the nanoantenna shows three clear features all of which are well reproduced by the simulation (Figure 2b, right panel): *i*) a bright spot in the center; *ii*) a bright ring, and *iii*) four bright spots decorating the edges. We explain this complex pattern in the near-field images by the interference of individual modes, simultaneously excited due to their spectral overlap for different dipole locations (simulated spectra in Figure 2a). To

disentangle the individual modes from this interference pattern, we calculate the spatial near-field distribution above the nanoantenna at the resonant frequencies around ω_0=1480 cm^{-1} (cyan line in Figure 2a), as shown in Figure 2c. When the dipole is located at the center of the nanoantenna, we observe a "breathing" mode (c1 mode, top left in Figure 2c), which explains the bright spot and bright ring obtained in the experimental near-field image at ω_0=1480 cm^{-1} (Figure 2b, left panel). When the dipole is located at the corner of the nanoantenna, a completely different mode appears (e2 mode, top right in Figure 2c) with field oscillations strongly confined to the edge, revealing the excitation of hyperbolic surface PhPs whose interference with the dipole field produces bright and dark dots along the edges of the nanoantenna as the result of a Fano-like resonance[46]. When the dipole is located at the flank of the nanoantenna (Figure 2c, bottom left) or at its diagonal (Figure 2c, bottom right), we can distinguish the modes s2 and d2 in the field pattern exhibiting a funnel-like shape or four-lobes, respectively. Thus, by locating the dipole at these representative positions above the h-BN square nanoantenna, we show that the combination of four individual modes (c1, e2, s2, d2) can explain the experimental near-field image taken at ω_0=1480 cm^{-1} (Figure 2b). The interference of these narrow Fabry-Perot resonances explains the complex near-field patterns obtained in our square h-BN nanoantennas, which yield "hot spots" with deeply subwavelength volumes as small as ~150×150×100 nm^3 (Figure 2b).
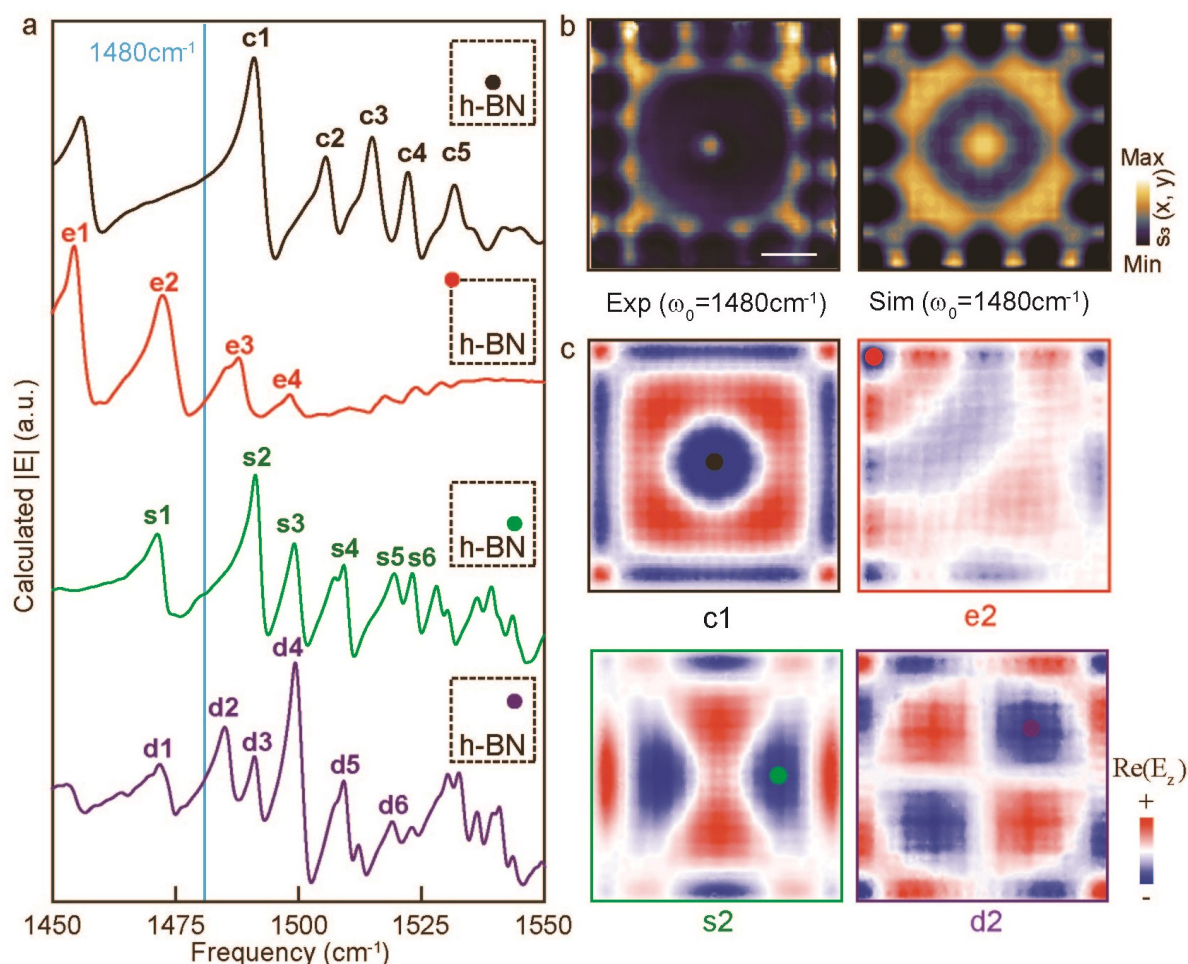
Figure 2. Analysis of the polaritonic modes excited in a square h-BN nanoantenna. (a) Simulated near-field spectra obtained by placing a point-dipole source at the nanoantenna center (black), corner (red), flank (green), and diagonal (purple), as indicated by the schematics (dashed square) in each case. The cyan and orange vertical lines represent the incident frequencies $\omega_0 = 1480 cm^{-1}$ and $\omega_0 = 1500 cm^{-1}$, respectively. (b) Experimental (left panel) and calculated (right panel) complex near-field patterns in a square h-BN nanoantenna at $\omega_0 = 1480 cm^{-1}$. (c) The field distributions for the calculated individual modes at the frequencies of the corresponding peaks: c1 (top left), e2 (top right), s2 (bottom left) and d2 (bottom right) in correspondence with (a). Scale bar: 500 nm.

4. Passive tuning of the polaritonic resonances in a square h-BN nanoantenna by tailoring its dielectric environment.

Since polaritons extend as evanescent waves into the media above and below polaritonic nanoantennas, their wavelength is sensitive to the dielectric properties of both the substrate and superstrate. Passive tuning of dispersion of propagating PhPs has been reported with substrate [41,47] and superstrate engineering[48], yet such tuning of narrow resonances in an individual phononic nanoantenna has never been realized, in spite of its important roles as building blocks in optical circuitry. To do that, we transfer one and the same square h-BN nanoantenna (see details in Methods) on two common substrates: silica (SiO_2) and silicon carbide (4H-SiC). At ω_0=1480 cm^{-1}, the complex values of the permittivity for SiO_2 and SiC are ε_{SiO_2} =2.01+0.01i and ε_{SiC} =5.50+0.005i, respectively. Within the regime of a small loss tangent ($Im(\varepsilon)/Re(\varepsilon) < 0.1$) [47], we can neglect the influence on the nanoantenna response of the optical losses of these substrates. The near-field images taken at ω_0=1480 cm^{-1} for the nanoantenna placed on SiO_2 and SiC present significant differences (**Figure 3**). Indeed, a prominent bright spot (Figure 3a) in the center of the nanoantenna on SiO_2 strongly contrasts with a dark spot surrounded by a bright circle (Figure 3b) of the nanoantenna on SiC. Likewise, the number of bright spots along the edges increases from four (Figure 3a) for the SiO_2 substrate to five (Figure 3b) for SiC, clearly indicating that hyperbolic surface polaritons are also very sensitive to the permittivity of the substrate. In contrast to previous spectroscopic measurements in phononic nanoantennas[28], these images reveal varying PhP modes as a result of the different dielectric nature of the substrate, thus demonstrating passive tuning of the nanoantenna resonances. Notice that the near-field image taken at ω_0=1480 cm^{-1} of the

nanoantenna on SiC (Figure 3b) appears to be similar to that at ω_0=1500 cm^{-1} for the nanoantenna on SiO$_2$ (Figure 2c), indicating that at a fixed ω_0 the PhPs wavelength in h-BN/SiC is smaller than that in h-BN/SiO$_2$, thus implying a red-shift of the resonances in the nanoantenna. To further elaborate on this frequency shift, we perform nanoimaging spectroscopy at the center of the square h-BN nanoantenna by recording the near-field amplitude at fixed illuminating frequencies (see details in Methods). The green and blue symbols in Figure 3c represent the experimental results for the nanoantenna on SiO$_2$ and SiC respectively, showing a good quantitative agreement with the simulated spectra (solid lines in Figure 3c). We observe a clear red-shift of the resonant peaks when the substrate is changed from SiO$_2$ (black solid line in Figure 3c) to SiC (orange solid line in Figure 3c). Specifically, for the same c1 mode (the field distribution can be found in the insets to Figure 3c), the resonant frequency (ω_{res-c1}) changes from ~1492 cm^{-1} to ~1458 cm^{-1}. Such red-shift can be explained by the general rule of a higher refractive-index substrate (SiC) to sustain polaritons with smaller wavelength[47], which agrees well with our near-field images. We further characterize the quality factor, $Q=\frac{\omega_{res}}{\Delta\omega_{res}}$, where ω_{res} and $\Delta\omega_{res}$ represent the resonant frequency and linewidth of our square h-BN nanoantennas. By fitting the experimental results (green solid symbols in Figure 3c) and taking into account the asymmetric Fano-like shape of the resonant peaks, we approximately estimate (Figure S5) a linewidth of ~9 cm^{-1} for the peak corresponding to the c1 mode, which yields Q~165. This value is comparable to those extracted for other types of phononic nanoantennas[26, 28, 35] and is much higher than those of typical metallic nanoantennas[49] in the mid-IR range. More importantly, such high Q is accompanied by an extreme sub-wavelength confinement (~λ_0/42), thus providing an excellent playground for experiments on strong light-matter interactions.
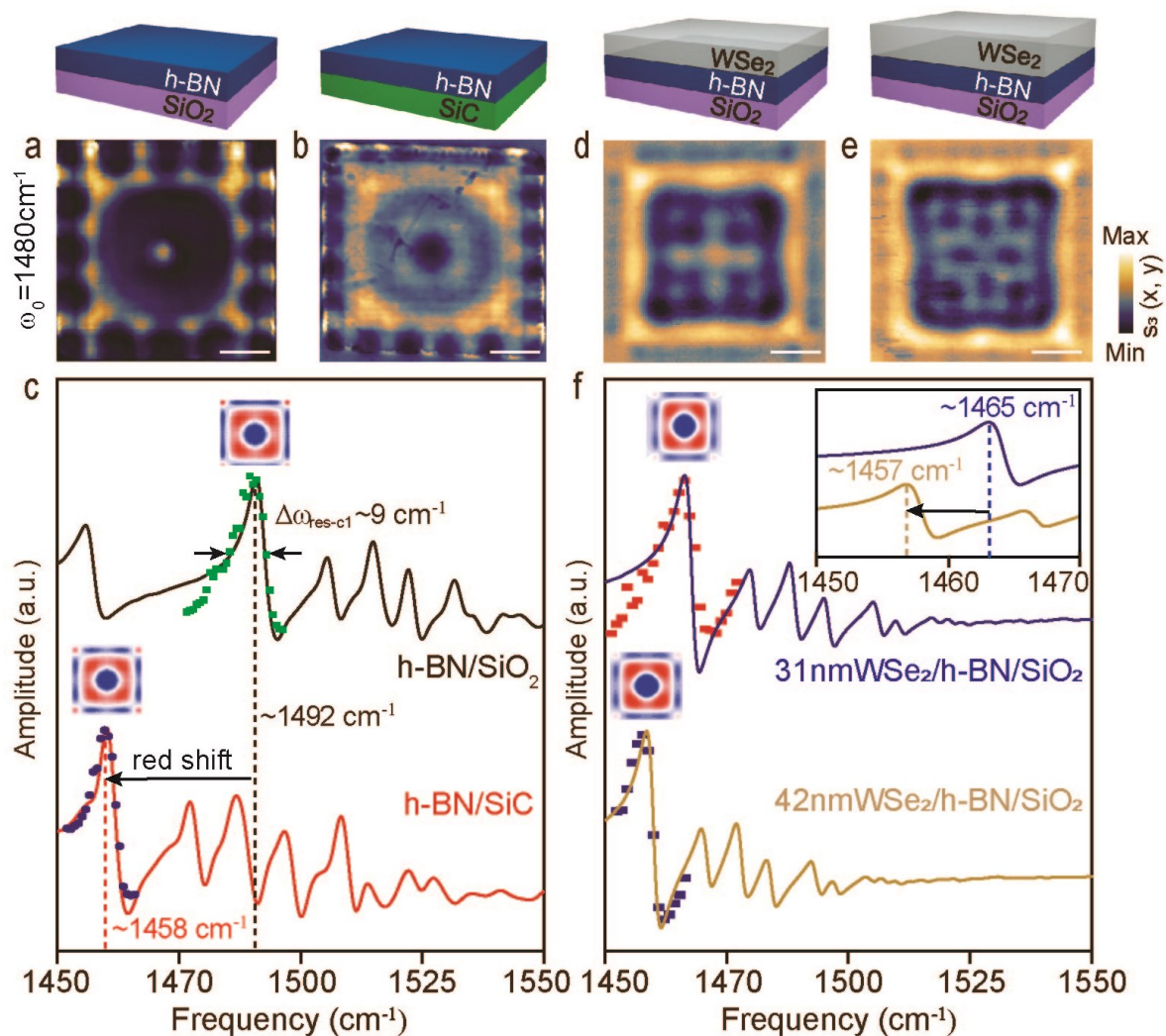
Figure 3. Passive tuning of the polaritonic resonances in a square h-BN nanoantenna by tailoring its dielectric environment. (a, b) Near-field images of a square h-BN nanoantenna taken at $\omega_0=1480cm^{-1}$ when it is placed on SiO_2 (a) and SiC (b). (c) Calculated near-field spectra for the cases shown in (a) (black solid line) and (b) (red solid line), respectively. The green and blue dots represent the experimental results in each case. The insets show the calculated field distributions at the resonance peaks corresponding to the c1 mode at $\omega_0=1492cm^{-1}$ and $\omega_0=1458cm^{-1}$ for the nanoantenna placed on SiO_2 and SiC, respectively. (d, e) Near-field images of the nanoantenna taken at $\omega_0=1480cm^{-1}$ when it is placed SiO_2 and covered with a layer of WSe_2 with thickness of 31 nm (d) and 42nm (e). (f) Calculated near-field spectra for the cases shown in (d) (blue solid line) and (e) (brown solid line). The red and blue dots represent the experimental results in each case. The insets show the calculated field distribution at the resonance peaks corresponding to the c1 mode at $\omega_0=1465cm^{-1}$

and ω_0=1457cm^{-1} for the cases shown in (d), and (e). The zoomed near-field spectra spanning 1450cm^{-1}-1470cm^{-1} in the inset demonstrate a clear red-shift for the resonance peak corresponding to the c1 mode. Scale bar: 500 nm.

Yet, from a practical perspective, it is much more advantageous to realize passive tuning of the nanoantenna resonances by varying the superstrate rather than the substrate, since by doing so one can control the PhP modes without moving the nanoantenna. To investigate the modulation of the nanoantenna polaritonic response by changing the superstrate, we cover a square h-BN nanoantenna with thin slabs of WSe$_2$, which exhibits a high dielectric index (Re (ε_{WSe2}) ~14) in the mid-IR spectral range[50]. As shown in Figure 3d, the near-field pattern in the nanoantenna drastically changes after covering it with a 31-nm-thick layer of WSe$_2$ (Figure 3a). The pattern strongly changes as well when we put another 11-nm-thick layer of WSe$_2$ on top (Figure 3e), so that the nanoantenna gets covered by a superstrate layer with a total thickness of 42-nm. The near-field images of the nanoantennas covered with 31-nm- and 42-nm-thick layers of WSe$_2$ at ω_0=1480 cm^{-1} are similar to the ones of the bare nanoantenna at ω_0=1520 cm^{-1} (Figure 1g) and ω_0=1530 cm^{-1} (Figure 1h), respectively. This indicates that at a fixed ω_0 the PhPs wavelength in WSe$_2$-covered h-BN is smaller than that in bare h-BN, thus implying a red-shift of the resonances in the square h-BN nanoantennas. To further elaborate on this frequency shift, we perform nanoimaging spectroscopy at the center of the square nanoantenna by recording the near-field amplitude at fixed illuminating frequencies. The red and blue symbols in Figure 3f represent the experimental results for the nanoantenna covered with 31 nm and 42 nm of WSe$_2$, respectively. A good quantitative agreement with the simulated spectra (solid lines in Figure 3f) is obtained. There is a clear red-shift of the resonant peaks when the thickness of the WSe$_2$ layers changes from 31 nm (blue solid line in Figure 3f) to 42 nm (brown solid

line in Figure 3f). Since $Re(\varepsilon_{WSe2})$ is much larger than 1, such red-shift is analogous to the shift obtained when transferring the nanoantenna from a low-refractive index to a high-refractive index substrate, *e.g.* from SiO_2 to SiC (Figure 3a-3b). Specifically, the peak corresponding to the c1 mode (field distribution in the insets in Figure 3f) shifts from ω_{res-c1}~1492 cm^{-1} for h-BN/SiO$_2$, to ω_{res-c1}~1465 cm^{-1} for 31-nm WSe$_2$/hBN/SiO$_2$, and finally to ω_{res-c1}~1457 cm^{-1} for 42-nm WSe$_2$/hBN/SiO$_2$. Altogether, our infrared nanospectroscopy and nanoimaging experiments, reveal that low-loss resonances in phononic nanoantennas can be widely tuned by as much as 35 cm^{-1}, which is around four times the resonance linewidth (~9 cm^{-1}), by varying dynamically the superstrate of the nanoantennas.

5. Active tuning of a polaritonic resonance in a square h-BN nanoantenna by electrostatic gating.

Although we demonstrate passive tuning of the polaritonic resonances in square h-BN nanoantennas in Figure 3, the challenge of active tuning of these resonances severely limits the technological implementation of phononic nanoantennas. One of the possibilities to actively tune the dispersion of propagating PhPs is to place h-BN slabs on top of a monolayer of graphene[38]. However, a dynamically tunable phononic nanoantenna, which can merge the merits of phononics (e.g. ultra-low losses) and graphene plasmonics (e.g. dynamically tuning capability), has never been reported. It is expected that the sharp PhP resonances in our nanoantennas can be controlled via electrostatic gating of a graphene layer placed below (see schematics in **Figure 4a**). By applying a back-gate voltage, we tune the carrier density and thus the Fermi level (E$_F$) in graphene (see details in Methods), from 0 to 0.25 eV. For the case of charge neutrality (E$_F$=0), the near-field image (Figure

4b, left panel) of the square nanoantenna taken at ω_0=1520 cm^{-1} exhibits a dark spot surrounded by a bright ring in the center, in good agreements with numerical simulations mimicking the experiment (Figure 4c, left panel). Remarkably, when E_F increases to 0.25 eV, the dark spot at the center of the nanoantenna both in the experimental and simulated near-field images transforms into a bright spot (right panels in Figure 4b and Figure 4c, respectively).
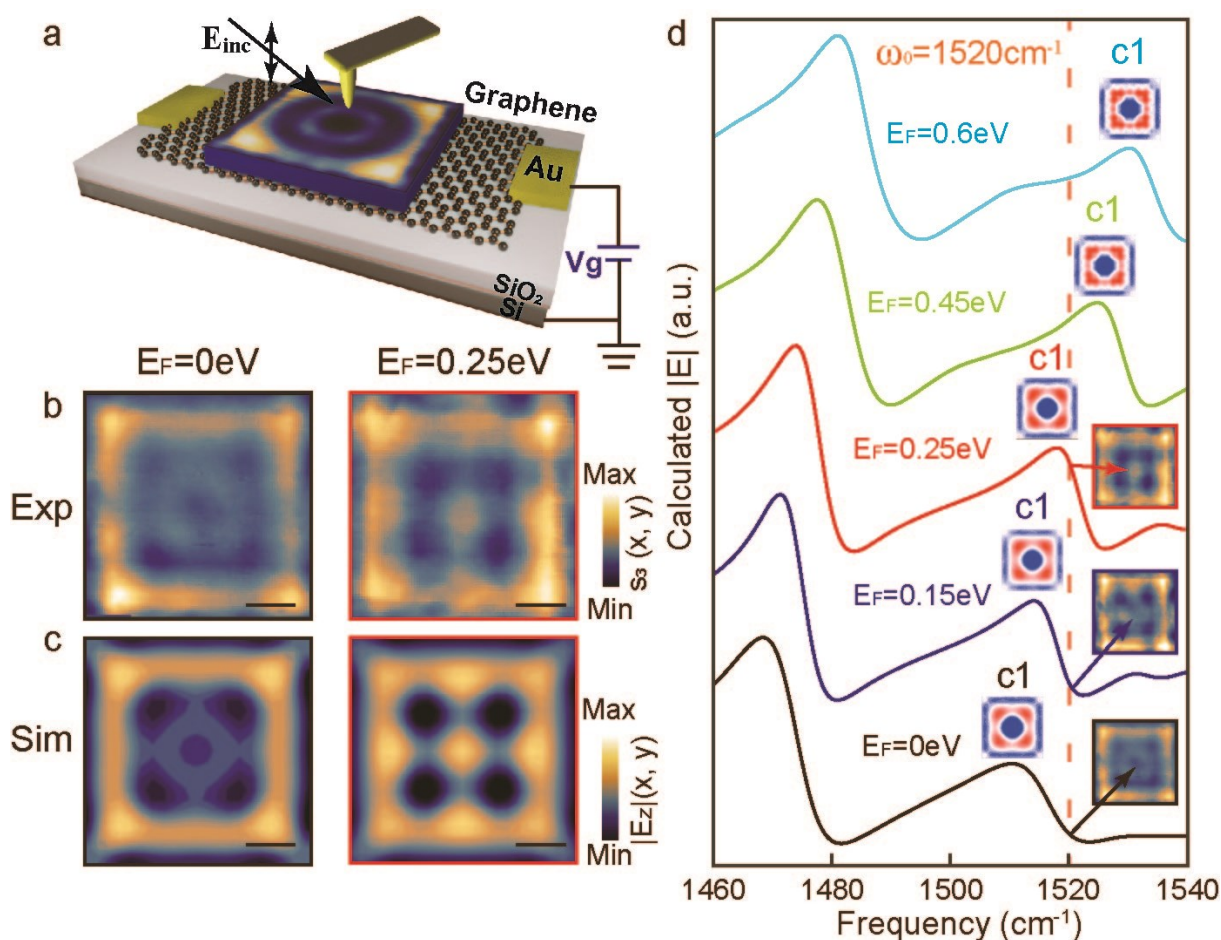

Figure 4 Active tuning of a polaritonic resonance in a square h-BN nanoantenna by electrostatic gating. (a) Schematics of the s-SNOM measurements of a square h-BN nanoantenna placed on top of a gated graphene layer. (b) Near-field images of the h-BN nanoantenna on top of graphene with Fermi levels E_F=0 eV (left panel) and E_F=0.25 eV (right panel). (c) Calculated images for the cases shown in (b). (d) Calculated near-field spectra of the square h-BN nanoantenna on top of graphene with Fermi levels E_F=0 eV (black solid line), E_F=0.15 eV (blue solid line), E_F=0.25 eV (red solid line),

E_F=0.45 eV (green solid line) and E_F=0.6 eV (cyan solid line). The insets represent the field distribution of the c1 mode at the shifted resonance peaks. The orange dashed vertical line represents the incident frequency ω_0=1520cm^{-1} in (b) and (c). When the resonace peak corresponding to the c1 mode is far from the incident frequency (e.g. E_F=0 eV and E_F=0.15 eV), the experimental near-field patterns (insets framed by black and blue squares) show a dark area in the center while it changes to a bright spot (inset framed by red square) for the case that c1-mode resonance peak is close to the incident frequency (e.g. E_F=0.25 eV). Scale bar: 250 nm.

Such a significant change of the near-field image provides a direct evidence of an active tuning of the PhP modes in the square h-BN nanoantenna at a fixed imaging frequency. We also corroborate the tuning of the spectral shift of the resonant modes in the nanoantenna by simulating the near-field spectra generated by a point dipole fixed at its center for different doping levels (Figure 4d). The resonant peaks experience a clear blue-shift with increasing E_F, specifically, the resonant frequency for the c1 mode (whose field distribution can be found in the insets in Figure 4d) shifts from ω_{res-c1}~1511 cm^{-1} for E_F=0 eV (black line in Figure 4d) to ω_{res-c1}~1518 cm^{-1} for E_F=0.25 eV (red line in Figure 4d), *i.e.* for moderately doped graphene. For heavily doped graphene (E_F=0.6 eV, cyan line in Figure 4d) it further shifts towards ω_{res-c1}~1530 cm^{-1}. As shown in the insets in Figure 4d, the exprimental near-field patterns show a dark area in the center of the h-BN nanoantenna for the case of E_F=0 eV and E_F=0.25 eV. However, it changes to a bright spot when E_F=0.25 eV. Given that the near-field signal in the center is mainly determined by the c1 mode (Figure 2), such change from dark to bright in the exprimental near-field images agrees well with the calculated near-field spectra, where the resonance peak corresponding to c1 mode gets closer and closer to the incident frequency (ω_0=1520 cm^{-1}) when E_F increases from 0 eV to 0.25. Note that the linewidths of these actively-tuned resonances ($\Delta\omega_{res}$~20 cm^{-1}) are larger than those in bare h-BN nanoantennas ($\Delta\omega_{res}$~9 cm^{-1}), which can be explained by the unavoidable introduction of ohmic losses due to the

presence of graphene. However, such linewidths are still more than one order of magnitude smaller than those typically obtained for IR plasmonic nanoantennas made of noble metals ($\Delta\omega_{res} >$400 cm^{-1}) [25] or graphene ($\Delta\omega_{res}\sim$200 cm^{-1}) [18]. We notice that such active tunability of PhP resonances in h-BN nanoantennas can be alternatively seen as a result of the coupling (hybridization) between graphene plasmon polaritons (GPPs) and PhPs (see Supplementary Figure 6). Such vision, goes in line with other recent experimental[38] and theoretical[51] studies.This result implies that our phononic nanoantennas combined with graphene not only relax the restriction of ohmic losses in graphene plasmonic nanoantennas but also preserve their dynamically tuning capability, thus paving the path for next-generation switchable integrated photonics devices at IR frequencies.

6. Conclusion

In conclusion, we report active and passive tuning of ultra-narrow polaritonic resonances in square h-BN nanoantennas. In particular, we demonstrate that these large-Q resonances can be effectively modulated over a wide spectral range by tailoring their dielectric environment passively, which is carried out by either placing them on different substrates, or simply covering them with nanometer-thick layers of WSe$_2$. More importantly, we demonstrate reversible in-situ (active) tuning of narrow resonances ($\Delta\omega_{res}\sim$20 cm^{-1}) in these nanoantennas when they are placed on top of a graphene layer, which promises applications based on tunable spectral selectivity or strong light-matter interactions. Furthermore, we find that the polaritonic modes associated with these dynamic resonances provide extraordinary near-field features such as a deep-subwavelength focus ($\sim\lambda_0/42$) of mid-IR light. Altogether, our results introduce tunable phononic nanoantennas as promising

building blocks for the development of IR nanodevices, including biosensors and narrowband thermal emitters.

7. Experimental Section/Methods

Sample Preparation: We fabricated the square h-BN nanoantennas by patterning boron-10 isotopically enriched h-BN flakes.[43] To do this, we first performed mechanical exfoliation from bulk h-BN materials using Nitto tape (Nitto Denko Co., SPV 224P). Afterwards, we performed a second exfoliation of the h-BN flakes from the initial tape to a transparent polydimethylsiloxane (PDMS) stamp. Subsequently, we transferred them onto a SiO_2/Si substrate using the dry transfer technique.[52] The square-shaped h-BN nanoantennas were defined in the h-BN flakes by high-resolution electron beam lithography.[45] To place the nanoantennas on different substrates, we picked them up using a stamp formed by a PDMS film covered with a layer of polypropylene carbonate (PC),[53] which was mounted in a micromanipulator. After the attached nanoantennas were precisely aligned and contacted on the target substrates, we heated them up to 200ºC in order to peel off the PDMS from the PC. Finally, to remove the PC layer, the sample was immersed into chloroform solvent at 70ºC. The same h-BN nanoantenna was covered with thin layers of WSe_2 (exfoliated using Nitto tape and PDMS stamp) with thicknesses of 31 nm and 11 nm, respectively.

Nanoimaging experiments: The nanoimaging experiments were performed using a commercial s-SNOM system (Neaspec GmbH) equipped with a quantum cascade laser (Daylight Solutions), spanning from 1400cm^{-1} to 1600cm^{-1}. The s-SNOM was based on an AFM operating in the tapping mode with Ω ~280 kHz and an amplitude of ~100nm. Commercial metal-coated (Pt/Ir) AFM tips

(ARROW-NCPt-50, Nanoworld) were employed. The sample was illuminated with a p-polarized mid-IR laser beam from the quantum cascade laser and the p-component of the tip-scattered light was collected with a parabolic mirror. To effectively suppress the background, the detected signals were demodulated at the 3rd harmonic. Pseudoheterodyne interferometry was employed to extract both the amplitude and the phase of the near field.

Numerical simulations of s-SNOM images, near-field spectra and mode dispersions: We performed the full-wave numerical simulations shown in Figure 2-4 by using a finite element method (COMSOL). In the simulated model, we approximated the AFM tip by a vertically oriented electric dipole source. We assume that the vertical component of the electric field ($|E_z|$) below the dipole mimics the near-field signal detected in s-SNOM measurements. This simple model has shown an excellent agreement with the experiment for both graphene nanoresonators[46] and h-BN linear antennas[26].

For reproducing the experimental near-field images, we scanned the dipole above the square h-BN nanoantennas at a fixed imaging frequency ω_0, recorded $|E_z|$ as a function of the dipole position, and obtained the simulated near-field images (Figure 2b-2c, Figure 4c). For calculating the near-field spectra (Figure 2a, Figure 3c, Figure 3f, Figure 4d), we located the dipole at one fixed position and calculated $|E_z|$ as a function of ω_0. For analyzing the electric field distribution of individual modes (Figure 2b-2c, insets in Figure 3c, Figure 3f, and Figure 4d), we calculated Re (E_z) in *x-y* plane 30-nm above the h-BN nanoantennas at a fixed dipole position and imaging frequency. In all simulations, the height of the dipole above the nanoantennas was fixed to 300 nm. The simulations of the covered nanoantennas considered that the upper WSe_2 layer is not in contact with the sidewalls of the nanoantennas. For calculating the dispersions of the M0 and SM0 modes (Figure 1f), we

employed the quasi-normal mode analysis implemented in COMSOL and considered both the material anisotropy and losses. From the mode analysis we obtained the complex wavevectors of the PhPs, along with their electromagnetic field distributions.

Model for graphene conductivity and electrostatic tuning of the chemical potential: Within the random phase approximation, the graphene conductivity can be expressed as a sum of the intraband and interband contributions:[54, 55]

$$\sigma = \sigma_{intra} + \sigma_{inter}. \tag{1}$$

The intraband and interband contributions read:

$$\sigma_{intra} = \frac{2ie^2t}{\hbar\pi\Omega}\ln\left[2\cosh(\frac{1}{2t})\right]. \tag{2}$$

$$\sigma_{inter} = \frac{e^2}{4\hbar}\left[\frac{1}{2} + \frac{1}{pi}\arctan\left(\frac{\Omega-2}{2t}\right) - \frac{i}{2\pi}\ln\frac{(\Omega+2)^2}{(\Omega-2)^2+(2t)^2}\right]. \tag{3}$$

Where $\Omega = \hbar\omega/\mu$, $t = T/\mu$, and μ is the chemical potential, with temperature *T* expressed in units of energy. A finite relaxation time can be taken into account by substituting ω by $\omega + i\tau^{-1}$ in σ_{intra}

The chemical potential of graphene depends upon transverse electric field via a DC biased gated structure, thus allowing for an active tuning of the graphene conductivity. The applied DC voltage (V_{DC}) modifies the graphene carrier density (n_s) as:[56]

$$C_{ox}V_{DC} = q_e n_s. \tag{4}$$

Where $C_{ox} = \epsilon_{SiO2}\epsilon_0/t$ is the gate capacitance, and ϵ_{SiO2} and t are the permittivity constant and the thickness of the SiO$_2$ that acts as a gate dielectric. This approximation is valid for small dielectric constants (such as that of SiO$_2$, $\epsilon_{SiO2} \sim 2$) and thicknesses larger than several nanometers

($t = 280$ nm in the measured sample). The carrier density is related to the chemical potential μ following the expression:

$$n_s = \frac{2}{\pi \hbar^2 v_f^2} \int_0^\infty \epsilon \left[f_d(\epsilon - \mu) - f_d(\epsilon + \mu) \right] d\epsilon. \tag{5}$$

where ϵ is the energy, v_f the Fermi velocity ($\sim 10^6 \, m/s$). By solving the previous two equations, an approximated closed-form expression that relates μ and V_{DC} can be obtained

$$\mu \approx \hbar v_f \sqrt{\frac{\pi C_{ox} V_{DC}}{q}}. \tag{6}$$

This expression was used to relate the capacitance measurements with the chemical potential of graphene.

Supporting Information

Supporting Information is available from the Wiley Online Library or from the author.

Author contributions

J.D. and P.A.-G. conceived the study. P.A.-G. and A.Y.N. supervised the project. J.D. fabricated the samples and carried out the near-field imaging measurements with the help of J.T.-G., I.D., A.B., A.I.F.T., and J.M.-S. F.J.A.M. conducted numerical simulations. D.A.B. and P.J-H. contributed to the fabrication of gated graphene samples. S.L. and J.H.E. provided the isotopically enriched boron nitride. P.A.-G., J.D., F.J.A.M., A.Y.N. and R.H. participated in data analysis. J.D., G.A.-P, F.J.A.M., A.Y.N., and P.A.-G. co-wrote the manuscript with input from the rest of authors.

Competing interests

R.H. is cofounder of Neaspec GmbH, a company producing scattering-type near-field scanning optical microscope systems, such as the one used in this study. The remaining authors declare no competing financial interests.

Received: ((will be filled in by the editorial staff))
Revised: ((will be filled in by the editorial staff))
Published online: ((will be filled in by the editorial staff))

References

[1] V. M. Agranovich, Surface polaritons, Elsevier, 2012

[2] D. Basov, M. Fogler, F. G. De Abajo, Science 2016, 354

[3] T. Low, A. Chaves, J. D. Caldwell, A. Kumar, N. X. Fang, P. Avouris, T. F. Heinz, F. Guinea, L. Martin-Moreno, F. Koppens, Nature materials 2017, 16, 182.

[4] I. Epstein, D. Alcaraz, Z. Huang, V.-V. Pusapati, J.-P. Hugonin, A. Kumar, X. M. Deputy, T. Khodkov, T. G. Rappoport, J.-Y. Hong, Science 2020, 368, 1219.

[5] H. Xu, E. J. Bjerneld, M. Käll, L. Börjesson, Physical review letters 1999, 83, 4357.

[6] R. Zhang, Y. Zhang, Z. Dong, S. Jiang, C. Zhang, L. Chen, L. Zhang, Y. Liao, J. Aizpurua, Y. e. Luo, Nature 2013, 498, 82.

[7] J. N. Anker, W. P. Hall, O. Lyandres, N. C. Shah, J. Zhao, R. P. Van Duyne, Nature Materials 2008, 7, 442.

[8] F. Koppens, T. Mueller, P. Avouris, A. Ferrari, M. Vitiello, M. Polini, Nature nanotechnology 2014, 9, 780.

[9] M. Schnell, P. Alonso-Gonzalez, L. Arzubiaga, F. Casanova, L. E. Hueso, A. Chuvilin, R. Hillenbrand, Nature photonics 2011, 5, 283.

[10] M. Schnell, A. García-Etxarri, A. Huber, K. Crozier, J. Aizpurua, R. Hillenbrand, Nature Photonics 2009, 3, 287.

[11] P. Roelli, C. Galland, N. Piro, T. J. Kippenberg, Nature nanotechnology 2016, 11, 164.

[12] H. Hu, X. Yang, X. Guo, K. Khaliji, S. R. Biswas, F. J. G. de Abajo, T. Low, Z. Sun, Q. Dai, Nature communications 2019, 10, 1;

[13] H. Hu, X. Yang, F. Zhai, D. Hu, R. Liu, K. Liu, Z. Sun, Q. Dai, Nature communications 2016, 7, 1;

[14] J. B. Khurgin, Nature nanotechnology 2015, 10, 2.

[15] G. Ni, d. A. McLeod, Z. Sun, L. Wang, L. Xiong, K. Post, S. Sunku, B.-Y. Jiang, J. Hone, C. R. Dean, Nature 2018, 557, 530;

[16] J. Chen, M. Badioli, P. Alonso-González, S. Thongrattanasiri, F. Huth, J. Osmond, M. Spasenović, A. Centeno, A. Pesquera, P. Godignon, Nature 2012, 487, 77.

[17] Z. Fei, A. Rodin, G. O. Andreev, W. Bao, A. McLeod, M. Wagner, L. Zhang, Z. Zhao, M. Thiemens, G. Dominguez, Nature 2012, 487, 82.

[18] D. Rodrigo, O. Limaj, D. Janner, D. Etezadi, F. J. G. De Abajo, V. Pruneri, H. Altug, Science 2015, 349, 165.

[19] L. Ju, B. Geng, J. Horng, C. Girit, M. Martin, Z. Hao, H. A. Bechtel, X. Liang, A. Zettl, Y. R. Shen, Nature nanotechnology 2011, 6, 630.

[20] H. Hu, F. Zhai, D. Hu, Z. Li, B. Bai, X. Yang, Q. Dai, Nanoscale 2015, 7, 19493;

[21] J. Duan, S. Xiao, J. Chen, Advanced Science 2019, 6, 1801974.

[22] F. H. Koppens, D. E. Chang, F. J. Garcia de Abajo, Nano letters 2011, 11, 3370.

[23]A. Woessner, M. B. Lundeberg, Y. Gao, A. Principi, P. Alonso-González, M. Carrega, K. Watanabe, T. Taniguchi, G. Vignale, M. Polini, Nature materials 2015, 14, 421;

[24] J. D. Caldwell, L. Lindsay, V. Giannini, I. Vurgaftman, T. L. Reinecke, S. A. Maier, O. J. Glembocki, Nanophotonics 2015, 4, 44.

[25] M. Autore, P. Li, I. Dolado, F. J. Alfaro-Mozaz, R. Esteban, A. Atxabal, F. Casanova, L. E. Hueso, P. Alonso-González, J. Aizpurua, Light: Science & Applications 2018, 7, 17172.

[26] F. Alfaro-Mozaz, P. Alonso-González, S. Vélez, I. Dolado, M. Autore, S. Mastel, F. Casanova, L. Hueso, P. Li, A. Y. Nikitin, Nature communications 2017, 8, 1.

[27] M. Tamagnone, K. Chaudhary, A. Zhu, M. Meretska, J. Li, J. H. Edgar, A. Ambrosio, F. Capasso, arXiv preprint arXiv:1905.02177 2019.

[28] M. Autore, I. Dolado, P. Li, R. Esteban, F. J. Alfaro‑Mozaz, A. Atxabal, S. Liu, J. H. Edgar, S. Vélez, F. Casanova, Advanced Optical Materials 2021, 9, 2001958.

[29] W. Ma, P. Alonso-González, S. Li, A. Y. Nikitin, J. Yuan, J. Martín-Sánchez, J. Taboada-Gutiérrez, I. Amenabar, P. Li, S. Vélez, Nature 2018, 562, 557.

[30] Z. Zheng, N. Xu, S. L. Oscurato, M. Tamagnone, F. Sun, Y. Jiang, Y. Ke, J. Chen, W. Huang, W. L. Wilson, Science advances 2019, 5, eaav8690.

[31] J. Taboada-Gutiérrez, G. Álvarez-Pérez, J. Duan, W. Ma, K. Crowley, I. Prieto, A. Bylinkin, M. Autore, H. Volkova, K. Kimura, Nature materials 2020, 19, 964.

[32] J. D. Caldwell, I. Aharonovich, G. Cassabois, J. H. Edgar, B. Gil, D. Basov, Nature Reviews Materials 2019, 4, 552.

[33] S. Dai, Q. Ma, T. Andersen, A. Mcleod, Z. Fei, M. Liu, M. Wagner, K. Watanabe, T. Taniguchi, M. Thiemens, Nature communications 2015, 6, 1;.

[34] P. Li, M. Lewin, A. V. Kretinin, J. D. Caldwell, K. S. Novoselov, T. Taniguchi, K. Watanabe, F. Gaussmann, T. Taubner, Nature communications 2015, 6, 1.

[35] J. D. Caldwell, A. V. Kretinin, Y. Chen, V. Giannini, M. M. Fogler, Y. Francescato, C. T. Ellis, J. G. Tischler, C. R. Woods, A. J. Giles, Nature communications 2014, 5, 1.

[36] F. Neubrech, C. Huck, K. Weber, A. Pucci, H. Giessen, Chemical reviews 2017, 117, 5110.

[37] F. Neubrech, A. Pucci, T. W. Cornelius, S. Karim, A. García-Etxarri, J. Aizpurua, Physical review letters 2008, 101, 157403.

[38] S. Dai, Q. Ma, M. Liu, T. Andersen, Z. Fei, M. Goldflam, M. Wagner, K. Watanabe, T. Taniguchi, M. Thiemens, Nature nanotechnology 2015, 10, 682.

[39] X. Yang, F. Zhai, H. Hu, D. Hu, R. Liu, S. Zhang, M. Sun, Z. Sun, J. Chen, Q. Dai, Advanced materials 2016, 28, 2931.

[40] S. Dai, Z. Fei, Q. Ma, A. Rodin, M. Wagner, A. McLeod, M. Liu, W. Gannett, W. Regan, K. Watanabe, Science 2014, 343, 1125.

[41] J. Duan, R. Chen, J. Li, K. Jin, Z. Sun, J. Chen, Advanced Materials 2017, 29, 1702494.

[42] P. Li, I. Dolado, F. Alfaro-Mozaz, A. Y. Nikitin, F. Casanova, L. Hueso, S. Vélez, R. Hcillenbrand, Nano letters 2017, 17, 228.

[43] A. J. Giles, S. Dai, I. Vurgaftman, T. Hoffman, S. Liu, L. Lindsay, C. T. Ellis, N. Assefa, I. Chatzakis, T. L. Reinecke, Nature materials 2018, 17, 134.

[44] Dai, S., Tymchenko, M., Yang, Y., Ma, Q., Pita-Vidal, M., Watanabe, K., Taniguchi, T., Jarillo‑Herrero, P., Fogler, M.M., Alù, A., Basov, D.N., Advanced Materials 2018, 30, 1706358.

[45] I. Dolado, F. J. Alfaro‑Mozaz, P. Li, E. Nikulina, A. Bylinkin, S. Liu, J. H. Edgar, F. Casanova, L. E. Hueso, P. Alonso‑González, Advanced Materials 2020, 32, 1906530.

[46] A. Nikitin, P. Alonso-González, S. Vélez, S. Mastel, A. Centeno, A. Pesquera, A. Zurutuza, F. Casanova, L. Hueso, F. Koppens, Nature Photonics 2016, 10, 239.

[47] A. Fali, S. T. White, T. G. Folland, M. He, N. A. Aghamiri, S. Liu, J. H. Edgar, J. D. Caldwell, R. F. Haglund, Y. Abate, Nano letters 2019, 19, 7725.

[48] Dubrovkin, A.M., Qiang, B., Salim, T., Nam, D., Zheludev, N.I. and Wang, Q.J., Nature Communications 2020, 11, 1863.

[49] J. B. Khurgin, G. Sun, Applied Physics Letters 2011, 99, 211106.

[50] F. L. Ruta, A. J. Sternbach, A. B. Dieng, A. S. McLeod, D. N. Basov, Nano Letters 2020, 20, 7933.

[51] Kumar, A., Low, T., Fung, K.H., Avouris, P. and Fang, N.X., Nano Letters 2015, 15, 3172.

[52] A. Castellanos-Gomez, M. Buscema, R. Molenaar, V. Singh, L. Janssen, H. S. Van Der Zant, G. A. Steele, 2D Materials 2014, 1, 011002.

[53] R. Frisenda, E. Navarro-Moratalla, P. Gant, D. P. De Lara, P. Jarillo-Herrero, R. V. Gorbachev, A. Castellanos-Gomez, Chemical Society Reviews 2018, 47, 53.

[54] A. Y. Nikitin, F. Guinea, F. Garcia-Vidal, L. Martin-Moreno, Physical Review B 2011, 84, 195446.

[55] B. Wunsch, T. Stauber, F. Sols, F. Guinea, New Journal of Physics 2006, 8, 318.

[56] J.-S. Gómez-Díaz, J. Perruisseau-Carrier, Optics express 2013, 21, 15490.

Near-field nanoscopy monitors active and passive tuning of ultra-narrow resonances in phononic nanoantennas over a wide spectral range (~35 cm^{-1}, being the resonance linewidth ~9 cm^{-1}). Passive tunability can be realized by tailoring the dielectric environment of nanoantennas made of boron nitride, while reversible in-situ tuning of narrow resonances is realized by placing nanoantennas on top of a graphene layer.